A&A, 707, A218 (2026)
https://doi.org/10.1051/0004-6361/202557540

Astronomy & Astrophysics

Gaia serial charge transfer inefficiency modelling and radiation damage study

C. Pagani[1,⋆], N. C. Hambly[2], M. Davidson[2], N. Rowell[2], C. Crowley[4], R. Collins[2], F. van Leeuwen[3], G. M. Seabroke[5], A. Holland[6], M. A. Barstow[1], and D. W. Evans[3]

[1] School of Physics and Astronomy, University of Leicester, University Road, Leicester LE1 7RH, UK
[2] Institute for Astronomy, School of Physics and Astronomy, University of Edinburgh, Royal Observatory, Blackford Hill, Edinburgh EH9 3HJ, UK
[3] Institute of Astronomy, University of Cambridge, Madingley Road, Cambridge CB3 0HA, UK
[4] HE Space Operations BV for ESA/ESAC, Camino Bajo del Castillo s/n, 28691 Villanueva de la Cañada, Spain
[5] Mullard Space Science Laboratory, University College London, Holmbury St Mary, Dorking, Surrey, RH5 6NT, UK
[6] The Open University, School of Physical Sciences, Centre for Electronic Imaging, Milton Keynes, UK

Received 3 October 2025 / Accepted 19 January 2026

ABSTRACT

During the course of its mission, ESA's *Gaia* spacecraft has generated a map of the stars of the Galaxy of exquisite detail. While in its L2 orbit, the satellite has been exposed to high-energy cosmic rays and solar particles, which caused permanent damage to its CCDs. The main effect of radiation damage on *Gaia* data is the distortion of its images and spectra that is caused by the charge transfer inefficiency (CTI) of the CCDs during the readout process. When this is not taken into account, it can result in inaccurate measurements of a star's location and flux. We analysed and modelled the effect of CTI on the serial readout direction, which is larger than in the parallel due to the presence of CCD manufacturing defects. A pixel-based physically motivated CTI model, `CtiPixel`, was developed to characterise the damage in *Gaia* CCDs. The model was calibrated using dedicated serial CTI diagnostic data, taken every three to four months over the course of the mission. The model is shown to be a good representation of the observed signatures of CTI in the calibration datasets, and its parameters reveal significant insights into the nature of the CCD defects generated by space irradiation. The damage in the serial direction slightly increases linearly over time in general, with sudden step changes after strong solar flares and coronal mass ejections directed towards Earth. The serial CTI showed a further step increase as a consequence of the engineering CCD annealing experiment that was carried out after the completion of *Gaia* science observations.

Key words. instrumentation: detectors – techniques: image processing – telescopes

1. Introduction

The *Gaia* satellite (Gaia Collaboration 2016), ESA's astrometric mission, was launched in December 2013 and collected data in its main science mode until January 2025, with the aim of creating the most detailed map of the stars of our Galaxy. The spacecraft operated in the vicinity of the second Lagrange point (L2), 1.5 million kilometers from Earth, and it scanned the sky by combining observations from the field of view of two telescopes that were separated by a basic angle of 106 degrees to measure the positions, distances, and proper motions of the stars with an accuracy of micro-arcseconds. In addition to the astrometric measurements, *Gaia* performed photometric observations of all detected sources, low-resolution spectrophotometry with the Blue and Red Photometers (BP and RP, and more generally referred to as XP devices) and near-infrared medium-resolution spectroscopy with the Radial-Velocity Spectrometer (RVS) for objects brighter than $G_{\rm RVS} \sim 16$.

Gaia's focal plane consists of a grid of 106 scientific e2v charge-coupled devices (CCDs; see Crowley et al. (2016b)). The detectors have been exposed to a high-energy particle environment since launch. The characteristics of this irradiation, based on measurements using *Gaia* detectors in combination with data from other spacecrafts in L2, is described and analysed in Crowley (in prep.). Over time, space irradiation causes permanent damage to the silicon structure of the detectors. The defects that are thus generated are also referred to as traps because they can cause the capture of electrons from a source signal and their release at a later time during the CCD readout process, which distorts the acquired images. This effect is quantified in terms of charge transfer inefficiency (CTI), defined as the fraction of charge that is lost to traps during the transfer of the signal from one pixel to the next (see e.g. Hopkinson et al. 1996). This was identified early on in the *Gaia* development phase as a critical aspect of the mission. For the fainter stars in particular, CTI can cause a distortion in the observed images that strongly affects the derivation of the detector position and flux of these stars.

After launch, the impact of CTI on *Gaia* data was found to be lower than originally anticipated by early radiation model studies, as shown in Crowley et al. (2016a). This was due to a number of factors. For instance, the timing of the launch, past solar maximum, and the low activity of the past solar cycle, proved beneficial in terms of total irradiation dose. Another mitigating effect on CTI for *Gaia* has been the overall higher than expected diffuse optical background component that reduces the impact of CTI during readout because its signal can keep some traps permanently occupied. In particular, in the along-scan (AL) direction, the accumulation of damage during the

⋆ Corresponding author: `cp232@le.ac.uk`

mission resulted in a parallel CTI that remained lower by a factor of ∼8 than the predictions. The serial CTI (sCTI) in the across-scan (AC) direction has slowly increased over the years, and it is higher in absolute terms than in the parallel direction. The main cause of sCTI is the manufacturing traps. These, already present at launch, affect the serial transfers to a higher degree than in the parallel direction because the serial readout timing is faster.

The focus of this paper is the analysis of the serial CTI effects on a set of *Gaia* engineering data that are taken periodically during the course of the mission, and the mapping of the damage evolution over time. In Sect. 2, we describe the telescope focal plane and its detectors, the L2 radiation environment, and the type of damage it causes on the CCDs. We review the preparatory work carried out before the satellite launch by the *Gaia* irradiation study team, aimed at predicting and modelling the effects of radiation in *Gaia* data. This analysis has informed the development of the `CtiPixel` CTI model and software package described in this paper. The model is based on the physical properties of the defects that cause CTI and their effects on charge during the detector readout process. `CtiPixel` was calibrated using a collection of dedicated serial CTI engineering activities, carried out periodically during the course of the mission, that involved the controlled injection of charge at the top of the CCDs. These engineering tasks and calibration datasets are presented in Sect. 3, while the `CtiPixel` model is described in Sect. 4. In Sect. 5 we present the method we used to process the serial calibration activities and to fit them with the `CtiPixel` model. The results of the fits are presented in Sect. 6. Finally, the physical interpretation of the fitted trap parameters, the limitations of the model, and an attempt to use `CtiPixel` to treat the signatures of serial CTI in *Gaia* science observations are discussed in Sect. 7. Appendix A presents the main effects on serial CTI following the CCD annealing procedure, which is one of the *Gaia* end-of-life (EoL) activities.

2. *Gaia* CCDs and radiation environment

The 106 detectors that form the *Gaia* focal plane are categorized by their function and properties, with the majority of them (62) identified as Astrometric Field (AF) CCDs, dedicated to the measurement of the position of the stars detected by the spacecraft Star Mapper (SM) devices (for a full description of the *Gaia* focal plane, see Kohley et al. (2014)). All detectors have image section dimensions of 4500 by 1966 pixels in the parallel and serial readout directions, with each pixel the physical size of 10×30 µm. The main difference between the devices employed in the focal plane is their thickness. For the AF and Blue Photometers (BP) CCDs, the thickness is 16 µm, while for the red variants employed in the RP and RVS detectors, a higher value of 40 µm enhances their sensitivity for sources emitting mainly at longer wavelengths.

2.1. CCD operations

The impact of radiation damage on the images and spectra acquired by a CCD depends both on the characteristics of the device and on how it is operated, for example on the timings of the readout process and the CCD temperature. A critical aspect for *Gaia* is the way its images are acquired, exposing the CCDs continuously while they are clocked in the parallel direction. This technique is known as Time Delayed Integration (or TDI) mode, in which the detectors are clocked in the parallel direction with a period of 0.9828 millisecond (corresponding to a clocking frequency of 1.017 kHz), matching the scanning rate of the stars over the detectors. Therefore, the signal from a transiting source is accumulated during the readout, in contrast to the typical CCD acquisition technique of exposing the camera at a fixed sky position for a determined amount of time followed by the readout of the frame.

The parallel transfer rate in TDI mode is rather long compared to that in more common CCD imaging. Furthermore, this is in stark contrast to the two-phase readout serial clocking frequency, which is extremely fast (10 MHz corresponding to charge transfer times of 0.1 µs in the serial register) except when samples are being read, yielding longer transfer times of order 10 µs upstream in the serial register. The fast-slow serial scan is further complicated by a readout suspension around the four-phase parallel clocking. This is because the video chain electronic offsets would be otherwise hugely disturbed during readout sampling by the voltage swings commanding those parallel phases (residual offset disturbances on resumption of the serial readout are presented in Hambly et al. (2018) where these aspects are discussed in greater detail). At each readout pause, the dwell time in the serial register, during which charge is confined under a pixel before being moved to the succeeding one is 80.4 µs for AF devices, and 76.8 µs for XP CCDs. Hence the serial scan consists mainly of about 2000 transfers of 0.1 µs, within which are scattered several tens of dwell times of 10 µs in contiguous groups (depending on instrument mode, allocation of science windows and of sacrificial braking samples used to further sample away the offset disturbances) plus three dwells of around 80 µs (one readout pause having taken place before the serial scan starts).

There are three other important characteristics of the *Gaia* CCDs that influence the effect of irradiation on its measurements. *Gaia*'s devices were designed and manufactured with pixels presenting a supplementary buried channel (SBC; Seabroke et al. 2013), which limits the volume within a pixel where the charge signal from a source is enclosed during readout, which reduces parallel CTI effects (the serial register has no SBC). The second is the charge injection functionality of the CCDs, in which a controlled amount of charge is injected at the top of the devices at specific intervals. During observations taken in normal science mode, a block of four contiguous lines are injected with approximately ten thousand electrons of charge per pixel every 2000 (AF mode) or 5000 (XP mode) lines. When these blocks of injected lines are readout they temporarily fill the defects of the entire CCDs with a fraction of their charge, mitigating the effects of CTI. Finally, of particular importance for CTI effects is the detectors' temperature. On *Gaia*, the nominal operating temperature of the CCDs is 163 K, with some variations of several degrees observed over the focal plane. The temperature has been found to be stable over time, albeit with low-level seasonal variations dependent on heliocentric distance in addition to abrupt variations in short intervals during specific mission phases such as the decontamination events and other disturbances to power dissipation in the focal plane array caused by operational changes (see Sect. 6.2).

2.2. Radiation environment at L2

The radiation environment experienced by *Gaia* at L2 is the focus of Crowley (in prep.). Its analysis is based on the data acquired by the 14 Star Mappers, the devices dedicated to the stars' on-board detections. In particular, as part of the automated detection algorithm, Prompt Particle Events (PPEs) are identified. These are features in the SM images that are too sharp

Table 1. Common silicon defect species.

Type	Symbol	Energy (eV)
Phosphorous	Si–E	0.44
Divacancy	V–V	0.41
Unknown		0.34
Multi-vacancy	V–V–V	0.20
Oxygen	Si–A	0.17

in comparison to the *Gaia* Point Spread Function shape to be considered true signals from point-like sources, and are instead attributed to high-energy particles, mostly protons, either cosmic rays or originating from the Sun. The observed PPEs rate can therefore be considered as a real-time measure of the radiation environment experienced by *Gaia*.

The impact of high-energy particles on the detectors can cause ionising or non-ionising radiation. In the first instance, irradiation is revealed over time as shifts in the measured CCD baseline voltage values (Srour & McGarrity 1988). This can be compensated by hardware setting adjustments during the course of the mission. The non-ionising radiation instead consists of the impact of high-energy particles with the silicon crystal of the detectors, that can lead to the displacement of one or multiple atoms from their original positions in the lattice structure, and is therefore also known as displacement damage (van Lint 1963); the atoms knocked out of their original sites leave a vacancy that can be filled over time by impurities already present in the detector, such as Phosphorous or Oxygen atoms (Watkins & Corbett 1964), or form a stable bonding with another vacancy (a type of defect called a divacancy; Marshall et al. 1989). These defects can become permanent, generating spurious energy levels between the valence and the conduction band of the semiconductor, where electrons can become temporarily trapped during the CCD readout process. The amount of time after which a trapped electron is released back into the conduction band is called the release (or emission) time, and it characterises the defect species, as it is a function of the specific trap energy level and the temperature at which the camera is operated. The trapping of electrons during the signal readout in CCDs is the cause of CTI, quantified as the fractional loss of charge during the transfer between two pixels. Common defects of silicon devices with their characteristic energy below the conduction band are listed in Table 1.

Onboard the *Gaia* spacecraft, the parallel CTI level and its evolution are monitored using the same blocks of Charge Injection (CI) lines that are used to mitigate the effect of radiation damage. The pixels following the blocks of CI lines present characteristic charge trails that are caused by the release of previously captured electrons in a stochastic process. The total charge in the trails provides a measurement of the number of active defects in the detector, and is a proxy for the CTI in the parallel direction. Figure 1 shows the measured intensity of the parallel trails, averaged over all the AF CCDs, for the entire span of the *Gaia* mission, with time expressed in units of On Board Mission Time (OBMT) revolutions, corresponding to approximately one satellite rotation (Lindegren et al. 2018). In the serial direction, a similar analyses is performed using the charge trails in the serial register post-scan pixels measured during dedicated serial CTI calibration datasets. These special engineering activities are described in detail in Sect. 3.

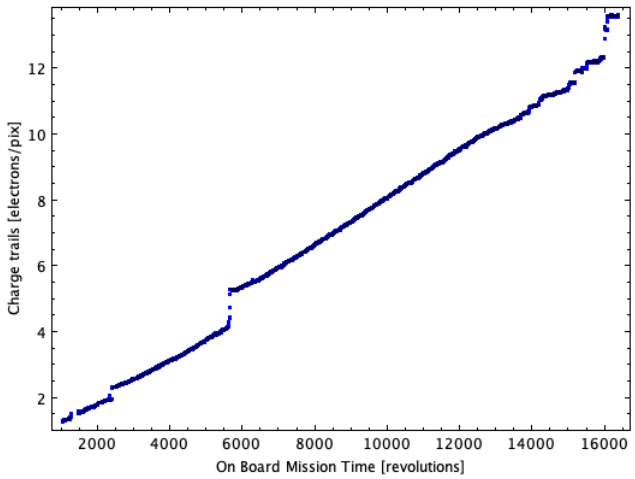

Fig. 1. Evolution of the measured charge trails intensity in the parallel direction averaged over all AF devices, covering the entire course of the *Gaia* mission. The trails are an empirical measure of the amount of radiation accumulated in orbit. The gradual increase in damage is caused by cosmic rays, while strong solar flares directed towards Earth cause the step changes in the damage evolution. Time intervals affected by temperature disturbances of the focal plan, due for example to decontamination activities or instances of incomplete telemetry, have been removed from the plot for clarity.

The analysis of the charge trails in *Gaia* CCDs has revealed a number of significant results that were first reported by Crowley et al. (2016b) using data from the initial two years of the mission. The measured evolution of the damage is characterised by a steady, gradual increase since the beginning of the mission that is attributed to the continuous irradiation from the Galactic Cosmic Rays (CR) flux (mostly protons and alpha particles). A second component of the damage evolution is seen as sudden steps at specific times in correspondence with significant solar activity events. The strongest of these occurred on the 10th of September 2017 (this correspond to an OBMT of 5651 revolutions), that saw a strong class X8.2 solar flare emitted in the Earth's direction (Seaton & Darnel 2018). The high-energy particles from that flare caused the generation of new defects in the detectors that resulted in a sudden increase of approximately 20% in the level of the charge trails.

A wealth of additional information can be derived from the analysis of the trails. For example, it can be seen that the gradual increase in the damage follows the 11-year modulation of the solar cycle, with a steeper accumulation rate during solar minimum and a shallower increase at solar maximum, in correspondence with the higher and lower levels of the measured Galactic CR flux. Another feature of the observed damage is its non-uniformity over the focal plane, due to the different amount of shielding from the irradiation and the mitigation effect of the local diffuse background signal. The analysis of the charge trails can reveal detailed information on the physical nature of the traps, such as the characteristic emission timescale of a specific defect type. This is described and discussed in the next Sects. 3 and 4.

3. *Gaia* serial CTI calibration activities

The radiation effect on the serial readout efficiency of the CCDs has been monitored throughout the course of the *Gaia* mission with a set of recurrent, dedicated serial CTI calibration

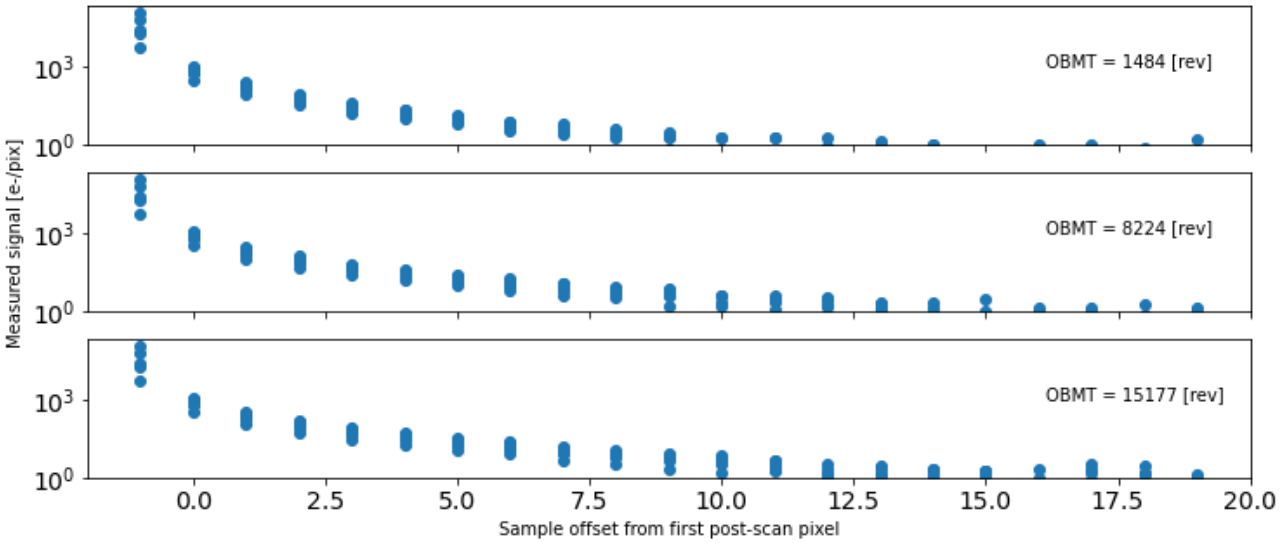

Fig. 2. Example charge trails from three epochs of *Gaia* in-orbit serial CTI calibration activities. The mean level of the charge injection in the image section CCD columns is shown before the start of the post-scan measurements illustrating the change of two orders of magnitude in the commanded blocks. A small increase in serial CTI is observed from early to late epochs in the mission time line, particularly for the release signature at longer timescales. These data come from device AF5 in row 5 near the middle of the focal plane array.

tests. These engineering activities, repeated every three to four months, comprise the injection of blocks of consecutive lines with charge at several intensity levels, regulated by the CCD injection voltage setting. At the lowest setting, the blocks are filled with approximately 10^3 electrons/pixel. During the activity, the voltage is raised a total of five times, reaching an injection level of up to a few hundred thousands of electrons per pixel. The full procedure results in five sets of data of increasing charge injection flux, each one of the five sets consisting of 70 blocks of 225 consecutive charge injected lines, followed by 200 lines with no injected charge. In a line, the injected charge value is not exactly the same in all pixels, but the charge pattern repeats line by line. Moreover, within a block, in spite of a constant commanded injection level, the actual signal falls slightly (a phenomenon known colloquially as injection droop).

When these engineering data are read out in the serial direction and the output node, the flux level of the final 12 pixels of the injected lines is recorded, along with the signal of 20 post-scan samples (24 for AF1 CCDs, the first strip of seven detectors of the AF devices). The post-scan pixels are virtual pixels, read out by over-clocking the serial register beyond the last image section column. Their signal follows an exponential decay (a trail), formed by deferred (or released) charge from previously trapped electrons, superposed on the electronic bias level of the video chain. The cumulative amount of signal in the post-scan samples, after subtraction of the CCD electronic offsets (the electronic bias), is an indicator of the density of traps in the serial register, and therefore of the amount of total irradiation and damage of the devices that is affecting the serial transfer process.

A total of 26 serial calibration activities has been carried out since the launch of *Gaia*. In Fig. 2 we show as an example the measured deferred charge levels in the post-scan pixels from three epochs of serial calibration activities, at each of the five charge signal levels, to illustrate the data input into the subsequent analyses. These measurements reveal a number of important aspects in regard to the damage. The shape of the charge trails in the post-scan pixels is reminiscent of a sum of exponential decays, regulated by the release timescales with which trapped charge is emitted from defect sites. Only specific trap species with an emission time of the same order as, or longer than, the serial clock period contribute to the observed trails. Faster traps will release the charge just captured within the same pixel, while the slower traps will release their charge on longer timescales compared to the CCD serial readout frequency. These data also display the effect of signal size on the amount of charge losses during readout. Larger amounts of injected charge occupy a bigger physical volume in the pixels, and can be affected by a higher number of traps, and lose more electrons during the charge transfers. Finally, the charge trails grow larger at later times during the mission. The integral under their curves corresponds to the total amount of charge released by traps after a line is readout into the first 20 following pixels, and the increase over time is a consequence of the accumulation of damage.

A dedicated serial CTI model was developed to process the serial calibration activities. The model is physically motivated, with the goal of extracting as much information as possible on the nature of the damage caused by space irradiation at L2. The model, named `CtiPixel`, and its calibration based on the engineering test data are presented in the following section.

4. The *Gaia* serial readout and CTI model, `CtiPixel`

In the years prior to launch, the *Gaia* Data Processing Consortium set up the *Gaia* Radiation Task Force, with the goal of developing the most effective model for the treatment of the effects of CTI on *Gaia* images. In the Task Force initial investigation, it soon became clear that to deal with the constraints posed by the very large volume of *Gaia* observations and the available computational resources, the only effective way to handle CTI without introducing a noise component of unknown characteristics in the data was through a forward modelling approach, in which the model of a source signal is distorted using the adopted CTI algorithm, and the derived damaged stellar profile is then compared to the measured flux of the source. The first CTI modelling implementation proposed by the Radiation Task Force was completely empirical, and was intended to be simple and therefore computationally fast, to be built upon over time with more

detailed and realistic models, closer to the true physical nature of the damage.

The most sophisticated model that followed the initial approach was named Charge Distortion Model 03, *CDM-03*. In *CDM-03*, the proposed analytical model (Short et al. 2013) is based on the physical theory of charge traps known as Shockley-Read-Hall (SRH; Shockley & Read 1952). Two aspects of this model are particularly important. Firstly, the process of capture of electrons by the traps is not assumed to be instantaneous, as in the case of more traditional CTI models, but instead follows a probabilistic mechanism that is a function of the number of electrons in the signal. Moreover, the concept of a density-driven regime to model the physical volume occupied by a signal charge cloud within a pixel was introduced in *CDM-03*. This was in contrast with the classical volume-driven CTI modelling, in which the occupied volume grows with the number of electrons in the signal. In the density-driven regime, the signal occupies all the available pixel volume, no matter its size. This choice was made to account for the results observed in *Gaia* irradiated devices before launch, that presented an unexpectedly large reduction in the measured CTI in the presence of a low, constant diffuse optical background. This was suggestive of the fact that the presence of a handful of electrons in each pixel of the detector had the effect of keeping the defects filled, mitigating the effects of CTI.

The CTI model developed for this work, named `CtiPixel`, inherits the fundamental principles on which the initial *Gaia* Radiation Task Force approach and the *CDM-03* model were based upon, and integrates them with tasks to closely reproduce the readout of charge signal in the serial register of *Gaia* CCDs. In particular, it implements a forward modelling treatment of the CTI effects and a physical characterisation of radiation damage, including the stochastic nature of charge trapping and release. It also includes the modelling of the impact on CTI of the scene, intended as the set of components present in the image in addition to the source signal itself, such as the one from other nearby stars or from straylight. The additional components have an impact on dynamics of the traps statistics, as for example a diffuse background signal can fill traps and lower the measured effects of CTI (this is known as the sacrificial charge effect). Finally, `CtiPixel` adopts a pixel based implementation, modelling the charge losses, the transfer of charge and the evolution of the trap statistics at the pixel level.

The choice of a physical model over a set of empirically derived functions has a number of important advantages. For instance, linking the model parameters to the physical properties of the damage makes their interpretation straightforward, giving insights into the nature of the defects that are generated by space irradiation; moreover, the parameters derived from a physical model are independent of the CCD operating modes and settings, and can be directly applied to different data types and scenarios. The choice of a pixel level implementation comes at the cost of a high demand in computational resources and processing time, but avoids simplifications and approximations, providing a benchmark CDM version of the highest accuracy.

`CtiPixel` has been employed to process the datasets acquired during the serial calibration activities that were described in Sect. 3. When the signal in the serial register line is processed the readout is simulated assuming an initial uniform charge injection flux over the entire serial register, calculated using a robust estimate of the measurements of the CI lines in a block, corrected by the residual bias evaluated from the prescan pixels. The sequence of serial transfer times for a specific CI line is retrieved using an utility that provides the dwell times (see previously) for the full readout process.

The modelling of the readout starts by shifting the charge by one pixel toward the readout node. For every pixel of the serial register, the `CtiPixel` processing task evaluates the charge losses due to the traps and the number of electrons released by each trap species into the pixel (L_i, and R_i, respectively, for the i_{th} trap species), and updates the total number of electrons F in the signal at pixel x accordingly,

$$F = F(x) + \sum_i (R_i - L_i). \tag{1}$$

In `CtiPixel` the capture and the release of electrons by traps is modelled as stochastic processes, with a capture probability P_c and emission probability P_e specific to each trap type. The probability of a trap capturing an electron in a time interval t is a function of the signal flux F in the pixel:

$$P_c = 1 - \mathrm{e}^{-\frac{t}{\tau_c}} = 1 - \mathrm{e}^{-\alpha t F^{\beta}}. \tag{2}$$

The capture parameter α in the above equation includes the trap cross-section σ, the thermal velocity of the electrons v_{th}, and the effective confinement volume V_c of the signal. The capture time constant τ_c is such that commonly, in classical radiation damage algorithms, the capture of an electron by a trap is assumed instantaneous ($P_c = 1$). In the case of *Gaia*, it is instead necessary to compute this probability explicitly, as its value can be smaller than one, in particular for the small charge packets of the faintest sources.

A defect can capture an electron if its location is within the physical volume occupied by the signal (its confinement volume V_c). The β parameter in Eq. (2) models how V_c varies as a function of the source signals size F, so that $\frac{V_c}{V_P} = (\frac{F}{FW})^{\beta}$, where V_P is the physical volume of the pixel and FW its full well capacity, in number of electrons. A β value of 1 is equivalent to the classic linear scaling of volume with number of electrons (the so called volume-driven model), while a $\beta = 0$ represents the regime in which a cloud of any size physically fills the entire pixel volume (the density-driven model mentioned earlier in the section).

The capture probability of the trap species i, $P_{c,i}$, (Eq. (2)), is used in `CtiPixel` to calculate the charge losses in a pixel in conjunction with the following quantities: the signal flux in the pixel $F(x)$, the fraction of the pixel's physical volume that the signal occupies ($V_f = V_c/V_P$), the density ρ_i of each species, and the fraction of empty traps ($f_{empty,i}$). To summarise, the total charge losses L in a pixel are therefore calculated as

$$L = \sum_i L_i = \sum_i F(x) V_f \rho_i f_{\mathrm{empty},i} P_{c,i}. \tag{3}$$

The probability of a defect emitting a previously trapped electron has a characteristics emission time τ_e,

$$P_e = 1 - \mathrm{e}^{-\frac{t}{\tau_e}}, \tag{4}$$

that is a function of the specific trap energy level E_t, the defect cross-section σ_n and the CCD operating temperature T, expressed as

$$\tau_e = \frac{\mathrm{e}^{\frac{E_t}{kT}}}{\chi \sigma_n v_{th} N_c}, \tag{5}$$

where χ is the entropy factor ($\simeq$1), v_{th} the thermal energy of the electrons and N_c are the number of effective states in the conduction band.

The emission (or release) time varies greatly among trap types, as its value is very sensitive to the characteristic energy level E_t of the species. Its measurement is therefore a very powerful method to identify the physical nature of the defect. Trap species like the O-Vacancy complex (or A-trap), with a characteristic energy of 0.17 eV or the multi-vacancy (V-V-V trap) at ≃0.20 eV, are expected to have the greatest impact on serial CTI in *Gaia* devices. At the nominal *Gaia* CCD temperature of –110 °C, using Eq. (5), the emission times of these species are of the order of a few to hundreds of microseconds, close to the serial readout sampling value. Other common species, like the Phosphorous-vacancy defect mentioned earlier, characterized by an energy level below the conduction band of approximately 0.44 eV, have emission times too long to affect the serial readout process. Once these defects capture an electron they remain filled for timescales much longer than the serial transfer process, and are said to be effectively frozen. These species have no net impact on serial CTI.

In the first attempts at fitting the serial calibration datasets using `CtiPixel`, a fixed, nominal CCD temperature of –110 °C was used for all the devices of the *Gaia* field of view. This was based on preliminary analysis of the spacecraft telemetry indicating a generally stable temperature over the field of view. A more detailed investigation of thermal variations has later shown differences of several degrees between devices and seasonal and long-scale fluctuations. Variation of up to 5 degrees in temperature over the field of view can lead to uncertainties in the estimates of the release timescale of fast trap species as the A-trap of up to 30% (see Eq. (5)). The updated CCD temperature information has subsequently been introduced to the fitting model. This change allowed the direct derivation of the characteristic energy level E_t of the species from the fits, in place of the temperature-dependent emission times τ_e.

In `CtiPixel`, the amount of previously captured charge by traps that is released back into a pixel is determined for each trap species by multiplying the release probabilities of Eq. (4) by the number of traps filled by captured electrons. The total number of electrons released into a pixel is therefore calculated as

$$R = \sum_i R_i = \sum_i \rho_i f_{\mathrm{filled},i} P_{e,i}, \tag{6}$$

where ρ_i is the number density of the i_{th} trap species, $f_{filled,i}$ is the fraction of traps filled with a captured electron for that species, and $P_{e,i}$ its emission probability.

`CtiPixel` simulates the serial readout process by updating the signal flux $F(x)$ of every pixel for the charge losses (Eq. (3)) and the charge released by each trap species (Eq. (1)) during a serial readout pixel clocking cycle, and tracking the defects statistics updating the number of empty and filled traps. The signal is then shifted by one pixel towards the readout node, and the calculations illustrated above are repeated, until the full readout register has been readout, and additionally evaluating the charge released by traps in the 20 (or 24 for AF1) post-scan pixels. At this stage, the flux of the bottom line from the CCD image section is transferred into the serial register, and the process is repeated until the serial readout of the full calibration dataset has been completed.

The parameters of `CtiPixel` that are fitted using the serial calibration activities datasets are the traps number densities ρ_i, the capture parameters α of Eq. (2) and the volume scaling β values, for each trap species. The parameter β is allowed to change by species to account for possible variations in the spacial distribution of the different impurities in the silicon. In addition, as mentioned earlier, during the initial fitting attempts the traps emission timescales τ_e (Eq. (5)) were also derived, employing the nominal *Gaia* temperature value of –110 °C for all devices and epochs. This choice was necessary as the complete telemetry from the temperature sensors over the *Gaia* focal plane wasn't available at the time the project was started and the initial model was being developed. In the refined `CtiPixel` implementation an epoch-dependent CCD temperature was used for each camera, derived from the spacecraft telemetry, allowing the direct fit of the characteristic energy level E_t of different species.

In the model, the trap species parameters τ_e (or E_t), α and β are set to be independent of time, as they are considered intrinsic characteristics of a defect type, while the traps number densities ρ_i are allowed to vary to track the increase of defects in the CCD caused by radiation. The capture parameter α can be converted into a characteristic capture cross-section σ of units cm^2 using the physical properties of the *Gaia* CCD pixels: their geometric volume V_g, the serial full well capacity FW of 475K electrons, and the thermal velocity of the electrons ($v_{th} \approx 1.21x10^7$ cm/s),

$$\sigma = \frac{2\alpha V_g}{v_{\mathrm{th}} \mathrm{FW}^{0.5}}. \tag{7}$$

The surface area of a readout register pixel is equal to 30 µm in the horizontal (H) direction, to match the width of the pixels in the image area, and 15 µm in the vertical (V) direction, larger compared to CCD image pixels (for a detailed description of the *Gaia* CCD architecture see Short et al. 2005).

This design allows serial pixels to handle a minimum of 2.5 times the full-well capacity of an image pixel. The depth (d) of the readout pixels was estimated at approximately 1 µm, based on pre-launch modelling and measurements by DPAC (private communication). The readout in the serial direction uses a two-phase scheme, and therefore, the signal packet cloud occupies one half of the pixel width at any one time, resulting in a total geometric volume $V_g = \mathrm{H} \times \mathrm{V} \times \mathrm{d} = \frac{30}{2} \times 15 \times 1\,\mu m^3 = 2.25 \times 10^{-10}$ cm^3, In the initial attempts at fitting the serial calibration datasets using `CtiPixel`, the number of trap species in the model was set to two, based on prior knowledge that both the Oxygen and the multi-vacancy defects could affect the serial readout in *Gaia* devices. The first fits results showed that this choice was not sufficient; on the contrary, it was found that a non-physical high number of trap species was required to achieve a satisfactory fit to the images. This was interpreted as a shortcoming of the model, and was tackled by introducing an additional process to the readout sequence: the possibility of re-capturing the electrons just released by previously filled traps within the same pixel. Charge re-capturing can be activated by setting a flag in `CtiPixel` . When the flag is set, the released charge is added to the signal flux of a pixel before the capture probability is computed. Charge re-capturing showed to improve the best-fit results, as will be presented in detail in Sect. 5.

The code in `CtiPixel` has been optimised and a set of numerical approximations was introduced to reduce the processing time of its computationally intense pixel-based implementation. The most significant optimisation is relative to the treatment of the pixels with a common input flux and the same traps state of the neighbouring pixels. These cases are recognised and flagged in the code so that the results of the model computations can be reused, avoiding unnecessary repetitions.

5. Serial post-scan trail fitting

The serial calibration activities have been performed a total of 26 times during the mission, with the first run at OBMT 1484

revolutions, and a final acquisition at OBMT revolution 16381, on the 14th of January 2025, shortly before the end of *Gaia* science operations. The data recorded from these activities consist of the measurement of the signal from a limited number of pixels: the final 12 CCD image area pixels of each line, to estimate the level of injected charge in the blocks, and the measurements in 20 (24 for devices in the first AF strip) post-scan pixels samples, that show the characteristic charge trails from the release of trapped electrons in the serial register. Data from all epochs have been fitted using the `CtiPixel` serial readout modelling task.

Within a block, the injected charge level is only approximately uniform, with the signal falling slightly from one line to the next despite a constant commanded injection voltage, due to the injection droop phenomenon. In our analyses, the signal from the 10^{th} line in a block is used to estimate the amount of injected charge, calculating the median of its values in the 70 blocks acquired at the same injection setting. The signal in the post-scan pixels must be evaluated precisely to detect levels of trailing charge as low as 0.1 electrons per pixel, on average. To this end, particular care has been given to accurately calibrate the electronic offsets, applying the required bias non-uniformity corrections (Hambly et al. 2018). The bias offset level for each pixel in the serial readout sequence is characterised using line scans made between the injection blocks with the first TDI blocking gate (Crowley et al. 2016b) in operation. Use of the gate ensures negligible photoelectric signal contamination to the offset values, but may introduce gate-dependent effects relative to the trail measurements that are made with no TDI gate active. The vector of offset values is measured relative to the final post-scan sample and then applied in conjunction with the prescan level on a line-by-line basis for the trail measurements. In this way any global gate-mode dependent effect is removed, although there likely remains some very low level of scan position dependent effects in the measurements. We note that in AF mode the 12th sample (9th in XP mode) in the post-scan trail sequences follows a readout pause and is subject to a large glitch offset (Hambly et al. 2018). Any inadequacies in the electronic offset correction manifest as a discontinuity in residual level from the 11th to the 12th trail sample in AF mode (8th to 9th in XP mode); in general no such discontinuity is observed but may be visible for one problematic device (see Sect. 6).

Two more lines of lower signal with respect to those of the five charge injection levels commanded in the blocks were included in the `CtiPixel` serial readout processing and the fits, with the goal of better constraining the model parameters. The signal in the lines immediately after a block are dominated by the typical exponential charge trails from parallel CTI due to traps present in the CCD image area that release electrons during the parallel readout. The first line of the release trail immediately following a block presents the highest such deferred signal, and therefore its serial trail charge in the serial post-scan pixels has the higher signal to noise when compared to the other lines following a block, but this was not employed in the analysis to avoid possible blooming charge contamination from the charge injection block. Instead, the signal from the second line following a charge injection block was preferred and added to the fits. Finally, the 100^{th} line after an injection block, dominated by the diffuse background signal integrated over 4500 TDI line transfers, was included in the fits. This line represents the lowest signal level in the fits.

The calibration datasets were fitted with the `CtiPixel` model employing standard non–linear least-squares minimisation using a Levenberg–Marquardt Algorithm (LMA) implementation. The fits were weighted by the inverse of the sample measurement variance, derived from a robust determination of the scatter of the input data. Initially the most problematic aspect of the fits were found to be the large excess residuals often seen in the first sample of the trails. Investigating this issue, evidence of charge blooming from the charge injection line into the neighbouring pixel was found in the case of red devices (RP and RVS CCDs), especially at the highest commanded injection voltage levels. To mitigate this effect, the flux values of the first sample in the case of the red devices has been corrected using the signal measured in the second pre-scan sample, i.e. that nearest the image section at the opposite end of the serial register. This of course assumes that any charge bleeds at the same rate forwards and backwards and affects only the pixels adjacent to the image section. In the case of the blue variant detectors (AF and BP CCDs) no evidence of any significant level of charge bleeding was found, and no correction of the signal in the first trails sample has been attempted.

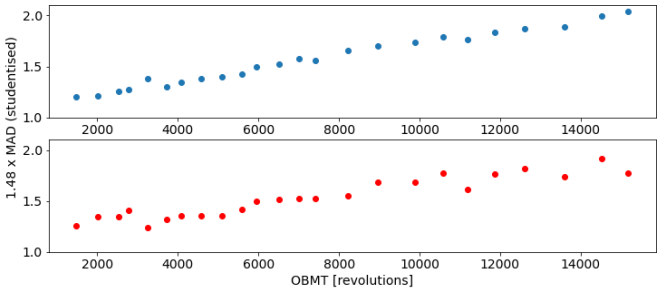

Fig. 3. Time evolution in the Gaussian-scaled median absolute deviation in unit-weight residuals, with time measured as OBMT for initial two-trap species calibrations fitting every device and epoch independently at an assumed constant focal plane operating temperature. The top panel shows all blue (AF and BP) devices, and the bottom panel shows RP devices.

6. Fit results

6.1. Initial calibrations

Visual inspection of the post-scan charge-release trails clearly indicates the need for multi-component decay curve modelling (see the deferred charge models as sum-of-exponentials in Hopkinson et al. (2005) and references therein), owing to the presence of trap species of different characteristic charge-release timescales. Initially, we chose a model with two trap species as a baseline to test the `CtiPixel` implementation and associated calibration procedure for all AF and XP devices. Each individual device and epoch was independently calibrated with a model having 7 free parameters: a single charge volume confinement parameter β common between the trap species, plus a trap density ρ, trap emission timescale τ_e (at an assumed constant nominal operating temperature in the focal plane) and trap capture cross-section parameter α for each of the two trap species. The results of these initial calibrations were rather unsatisfactory, with poor goodness-of-fits (GoFs) and clear evidence of systematic errors increasing with mission time. This is summarised in Fig. 3, which shows the robustly estimated unit-weight residuals of the entire calibrating dataset as a function of mission time, combined for all blue (AF and BP) and red (RP, but not including RVS) devices. The typical residual is ≈1.5 in both cases with a clear evolution as a function of time.

6.2. Final calibrations

The poor quality of the fits of the initial calibrations was addressed with a series of refinements to the `CtiPixel` model and the fit configuration. Specifically, two major changes were introduced: we increased the number of trap species to three, and implemented a more detailed treatment of the temperature of the CCDs, initially assumed constant over time and uniform over the field of view.

The introduction of a third trap species is justified by the gradual degradation with time in the quality of the initial two trap species calibrations. This indicates the emergence of a third defect species of significantly lower characteristic emission timescale, as radiation damage increased with mission time. Adding the third trap species to the fit improves the fit results, while the increased number of free parameters inevitably leads to higher levels of correlation and might render their physical interpretation more uncertain (this can be mitigated as further described below).

In the initial calibrations, the CCD temperature was assumed as fixed at the nominal focal plane value of 163 K. This simplification was not justified on close inspection of the FPA thermal measurements included in the spacecraft telemetry. A detailed investigation into the thermal properties of the focal plane revealed variation of many tenths of a degree over time for a specific device, in addition to differences of up to five degrees between CCDs. Figure 4 shows focal plane array temperature telemetry for the entire mission time line. Three thermistors are positioned on the FPA: with reference to the FPA device schematic in Fig. 1 of Crowley et al. (2016b), these are located on the lower left (row 1 SM), centrally (row 4 AF5) where the FPA is warmest, and on the upper right (row 7 RVS). The plot shows several interesting features:

- annual variation as solar irradiance changes with the Earth-Sun orbital distance;
- a secular change from cooler to warmer temperatures from the start of the mission to the end;
- very short time scale, large amplitude disturbances when operational changes cause large fluctuation in power dissipation (e.g. the step change near the end of mission when Proximity Electronics Module 4 failed on row 3 with the FPA subsequently stabilising at an operating temperature lowered by 0.3 K); and
- quantisation at the level of 0.05 K per ADU in the on-board analogue-to-digital converters reading the thermistor signals.
- large temperature variations induced by the mission EoL engineering tests.

The available telemetry was used to create an FPA temperature interpolation map by device position and mission time with the simplifying assumption of reflection symmetry to create a 2d temperature model from the limited positional coverage afforded by the FPA thermistors.

The incorrect assumption of a fixed temperature introduces significant scattering in the values derived for the fits of the parameter τ_e, the characteristic emission time of a trap species, due to the exponential in Eq. (5). As mentioned earlier, differences of 5 degrees over the focal plane can introduce uncertainties in the estimated release-time values of 30%, for a fast trap species like the ones that dominate CTI in the serial register, while a change of 1 degree over the course of the mission for a specific device can results in estimated trap emission time constants errors of almost 10%. In later implementations of `CtiPixel` and in the final calibrations the temperature of each

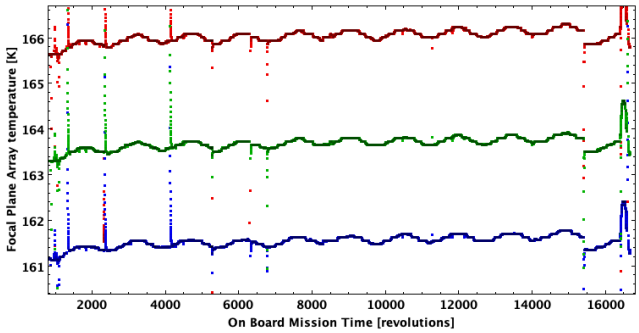

Fig. 4. Variation in the *Gaia* Focal Plane Array temperature over the course of the ten-year mission at three different positions: (blue) row 1 SM, (red) row 4 AF5, and (green) row 7 RVS.

device and its evolution during the epochs has been explicitly defined in the model. This choice also allows us to fit and directly derive the fundamental trap species energy level parameter E_t, instead of the release timescale τ_e.

Additional attempts to improve the fits by allowing a per-species charge volume confinement parameter β were limited in success. After some experimentation in configuration we settled on a three trap species model including per-species β but with the additional constraint of fitting for a single set of E_t, α and β common across all epochs on a device-by-device basis. The motivation was that for a given species we expect those trap parameters to be constant while the trap density ρ is free to evolve with time. Figures 5 to 7 illustrate the results for the three-trap species fits. Improvements were evident in the RMS and GoF histograms while the time evolution of the robustly estimated Gaussian-equivalent unit-weight calibration residual (in comparison with the same for the 2 trap, individual epoch calibrations shown in Fig. 3) was flattened significantly.

In Fig. 8, we show the time evolution in mean trap density for the three individual trap species modelled in the blue and red variant devices. We see clear evidence of a strong increase in the density of the higher-energy level traps (i.e. those with the longer timescales) with time, while the lowest energy level trap species remains relatively constant in both cases.

In order to investigate the robustness of our results we subdivided the measurement data into two sets covering the mission timeline, taking every odd or even epoch in the time-ordered sequence to provide two independent input datasets of the same size (13 epochs) covering the same overlapping time range. Figure 9 shows $y = x$ comparison plots for those trap parameters fixed across the epochs, which we expect to be the same within the uncertainties propagated through the weighted fits from the measurements, for the three trap species. The agreement is good for the dominant first species, fair for the second and somewhat less so for the third, although for many devices the agreement is reasonable across all trap types. This gives us some confidence that the trap parameters derived in the final calibrations have some useful level of physical reality despite the likely limitations of the fitting procedure. These include the arbitrary initialisation of the trap parameters in the non-linear least-squares optimisation, the possibility of hitting local minima in that process, and the high level of correlation between some parameters as expected from inspection of the model as formulated in Sect. 4.

The GoF distribution for the three-trap species fits (Fig. 6) indicates that the final model is a close representation of the data, although the median value is ≈1.5 rather than unity as might be expected under the assumption of normally distributed uncertainties. In order to examine potential systematic effects in

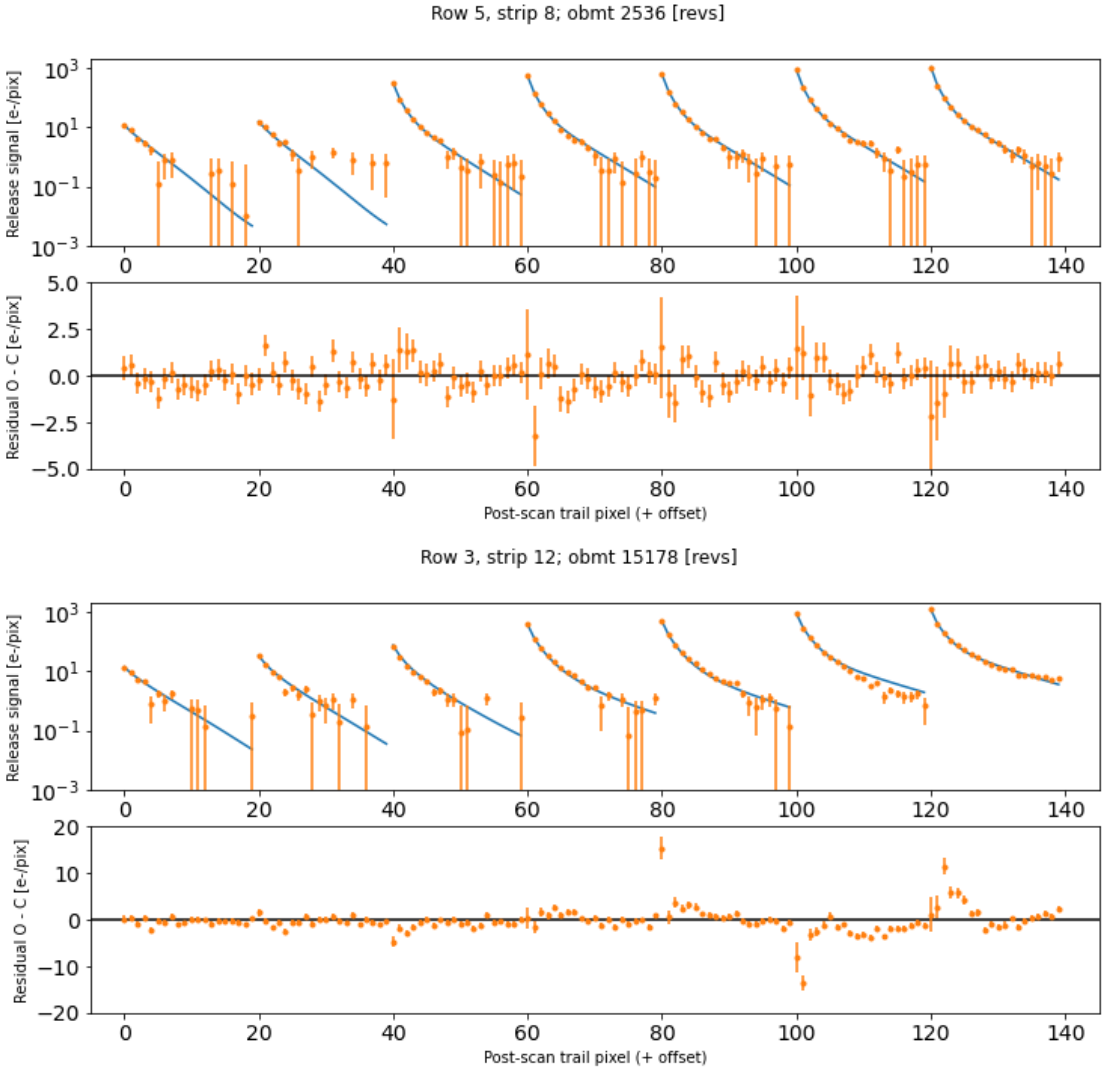

Fig. 5. Calibration data (orange points with measured uncertainties), final models (blue lines), and residuals for three-trap species `CtiPixel` models for two devices and epochs: A typical calibration for row 5, strip 8 (=AF5) near the start of the mission at OBMT 2536 revolutions (upper panels), and a poor example for row 3, strip 12 (=AF9) towards the end of the mission. The calibration data consist of seven individual post-scan trails, measured over a wide range in injected signal level, and having a length of 20 pixels each; they are shown concatenated in these plots for convenience.

more detail, in Fig. 10 we show scatter plots of the studentised residuals of the calibrations as a function of sample index in the postscan trails for the two CCD variants. These show evidence that the model is a little poorer in the very first pixels of the release curve following the injected signal block. This tendency of the `CtiPixel` model to follow less effectively the initial shape of the decay curves appears across all levels of the injected charge block so cannot be plausibly explained as poorly mitigated charge diffusion from large charge packets in the last pixel before the postscan samples. Otherwise, the only systematic effect clearly present is the residual bias non-uniformity discontinuity between samples 11 and 12 (blue), and 8 and 9 (red), which results from the presence of the readout freeze during the serial scan (Sect. 5).

7. Discussion of the results and insights into the physical nature of the radiation damage

The physically motivated representation of radiation damage in `CtiPixel` is of great advantage in the interpretation of the fits results, as it provides a direct link of the model parameters to the nature of the defects accumulated on *Gaia* CCDs over the course of the mission. At the same time, there are limitations with our analysis that should not be overlooked. The first one is that, while the results clearly show that the damage is composed of several defects types, with distinct charge-release times, only a limited number of post-scan pixels are available to fit the charge trails. This in turn limits the ability to constrain the fitting parameters, the release times (or trap energy levels) in particular, and can cause degeneracy between the trap parameters and possibly over-fitting, in case too many additional species are added to the model. Even more importantly, the simplifying assumption that the damage is composed of a small number of trap species with distinct energy levels might not be a realistic representation of the dynamical processes involved in the formation of defects in the *Gaia* space environment, as discussed below. Finally, as already mentioned earlier, the model doesn't appear to fit the very first trail samples perfectly, an effect that cannot be convincingly explained by an incorrect bias subtraction or by injected charge blooming from neighbouring pixels.

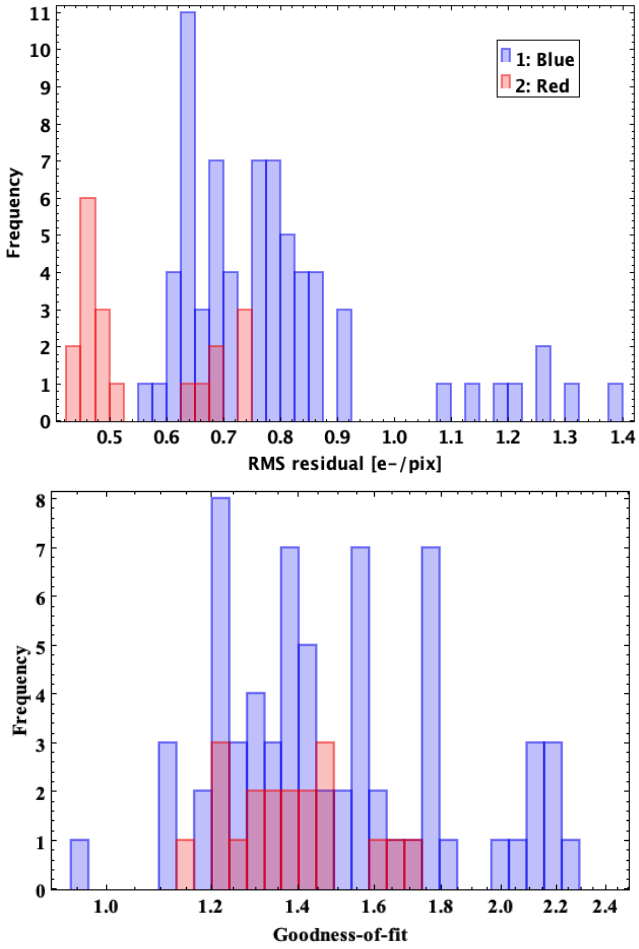

Fig. 6. Residuals (upper panel) and reduced χ^2 GoF (lower panel) histograms of 87 out of 88 (i.e. excluding AF9 in row 3) three-trap species `CtiPixel` final calibrations, subdivided into blue (AF and BP) and red variant (RP and RVS) samples (see text).

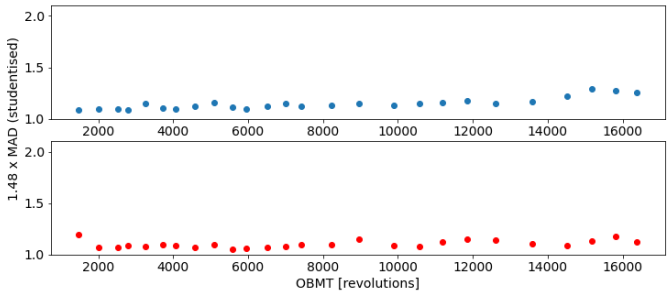

Fig. 7. Time evolution in the Gaussian-scaled median absolute deviation of the unit-weight residual with time measured as OBMT for the final three-trap species calibrations (compare the same for initial two-trap calibrations assuming fixed temperature in Fig. 3).

The clearest outcome of fitting the serial calibration datasets with `CtiPixel` is the emergence of new trap species in addition to the manufacturing Oxygen defect (the A-trap) that dominated the serial CTI of the *Gaia* CCDs at launch. As can be seen in Fig. 8, the density of the radiation-induced traps shows a general gradual increase, while small step changes can also be observed shorty after Coronal Mass Ejections directed towards Earth. Another significant step increase in serial CTI was observed in a dedicated calibration dataset collected after an engineering CCD

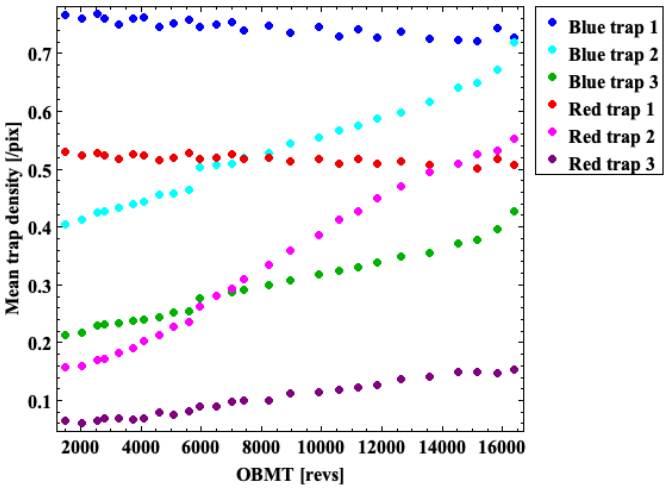

Fig. 8. Evolution of the mean trap density with time (measured as OBMT in units of the satellite revolution period of 6 hours) for the Blue (AF and BP) and Red (RP) CCDs, for the final three-trap species calibrations.

annealing activity, carried out after the final science observations were acquired. This result is discussed in Appendix A.

The new species generated by space radiation present higher energy levels and therefore longer emission timescales compared to the A-trap. Their peaks in the distribution of the trap release times can be clearly identified in Fig. 11. The intermediate trap species is characterised by an energy level of approximately 0.20 eV below the conduction band and emission time constant of 1.25×10^{-7} seconds at the CCD operating temperatures, suggestive of a possible association with the multi-vacancy defect. The slowest species peaks at approximately 6×10^{-7} seconds; interestingly, its distribution appears to have a tail of higher release-time values, extending as long as $\sim 10^{-5}$ seconds.

The origin of the wider distribution of characteristic energies and emission values of the third species could be in part attributed to poorly constrained best-fit parameters due to the relatively low density of this defect, especially early on in the mission. An alternative, plausible explanation is that the observed continuum is instead intrinsic to this type of defect at the time of the measurements, when the newly generated traps had not yet formed a stable bond with impurities or other vacancies in the lattice: in this case, the wide range of derived energy level values reflects their transitional state and the dynamics of the damage accumulation. A similar scenario has been experienced by the VIS CCDs (Euclid Collaboration: Cropper et al. 2025a) on board ESA's *Euclid* mission (Euclid Collaboration: Mellier et al. 2025b). The analysis of the damage experienced by the VIS CCDs during *Euclid*'s first year in space, measured using the trap pumping calibration technique (also known as pocket pumping (Janesick 2001; Hall et al. 2014)) showed a continuum of emission values for the newly developed traps (Skottfelt et al. 2024), just as seen in the `CtiPixel` model fits of *Gaia*'s damaged CCDs.

The clustering of the trap parameters for the distinct species can also be seen in the scatter plot of Fig. 12 for the final three-species fits. In this figure the fitted trap parameters α have been translated into a corresponding capture cross-section for each device at the appropriate operating temperature (see Eq. (7)). While the model parameters are evidently correlated, the plot illustrates the presence of at least two clearly distinct trap species populations, clustering at specific energy levels and cross-section values.

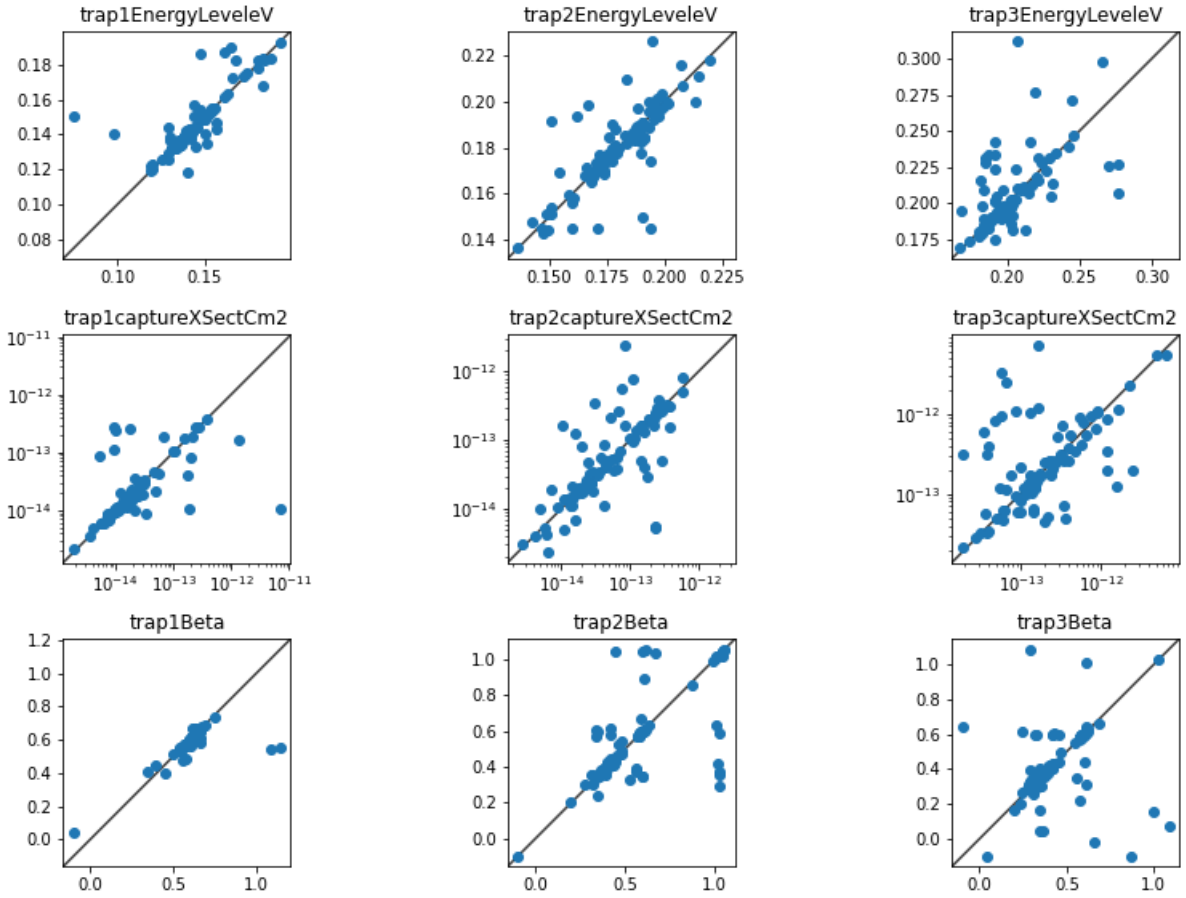

Fig. 9. Comparison of fitted trap parameters between two independent calibration runs combining every odd or even epoch dataset from the full time-ordered mission set (see text).

The evolution of the measured mean damage of Fig. 8 seems to suggest a slight decline in the number density of the A-type manufacturing species that dominated the defects at launch. This apparently surprising result is probably simply due to the degeneracy between the species' parameters when a third defect type is added to the fits. It is indeed unlikely that the observed trend could alternatively be caused, at least in part, to the physical process of annealing. Thermal annealing, resulting in the rearrangement of defects within the silicon lattice, happens quite quickly at high CCD temperatures, but in the cold environment of the *Gaia* focal plane any annealing process would be very slow, and therefore only contribute to the rearrangement of a very small fraction of defects.

Averaging the trap densities over all devices as shown in Fig. 8 risks hiding the finer details of the accumulation of defects in the *Gaia* devices. To more clearly reveal all aspects of the damage evolution, we present the example of CCD *(ROW3, AF6)*, positioned in the third row and sixth strip of AF devices in the focal plane in Fig. 13. The figure shows the combined number of defects per pixel of the three-trap species as a function of the number of revolutions since launch, as derived from the `CtiPixel` best fits. The general trend is dominated by a gradual accumulation of defects caused by the impact of Galactic cosmic rays on the detectors. As in the parallel case (Crowley et al. 2016a) the serial damage also shows step increases in data taken immediately following the strongest solar flares and coronal mass ejections of the last solar cycle. An interesting difference in the measured damage evolution between the two readout directions is observed in the magnitude of the step changes after the major flaring events in September 2017 and in the spring of 2024. The 2017 X8.2 class flare had the largest effect in the measured CTI in the image section (parallel readout direction), while in the serial register it resulted in a modest step increase of the total trap density. The opposite appears to be true after the 2024 period of strong solar activity. On further investigation, this surprising result has been attributed to the sudden temperature variation in the *Gaia* focal plane recorded in May 2024, that contributed to the changes in measured CTI. The colder operating temperatures have reduced its impact in the parallel direction, while in the serial register the readout losses have increased significantly. At this cooler setting the traps emission timescale have shifted to longer values (see Eq. (5)), impacting in opposite ways the ability of traps to capture electrons in the image section and the readout register, due to their different readout transfer frequencies.

Figure 14 shows fits parameters resulting from the fits of the entire set of serial calibration data available during the mission in the form of scatter plots and histograms. Outlying points from fits with GoFs on the tail of the distribution are not shown in the figure. In particular, the *(ROW3, AF9)* CCD is not well modelled by `CtiPixel`. This device presents a defect in column *AC*=1977 that might have caused the excess charge in the first post-scan pixel due to deferred charge that is causing poor fits of the charge trails, especially at high charge injection levels. We notice that *(ROW3, AF9)* is a twin CCD, one of 10 pairs of devices present in the *Gaia* focal plane (we use the term twins

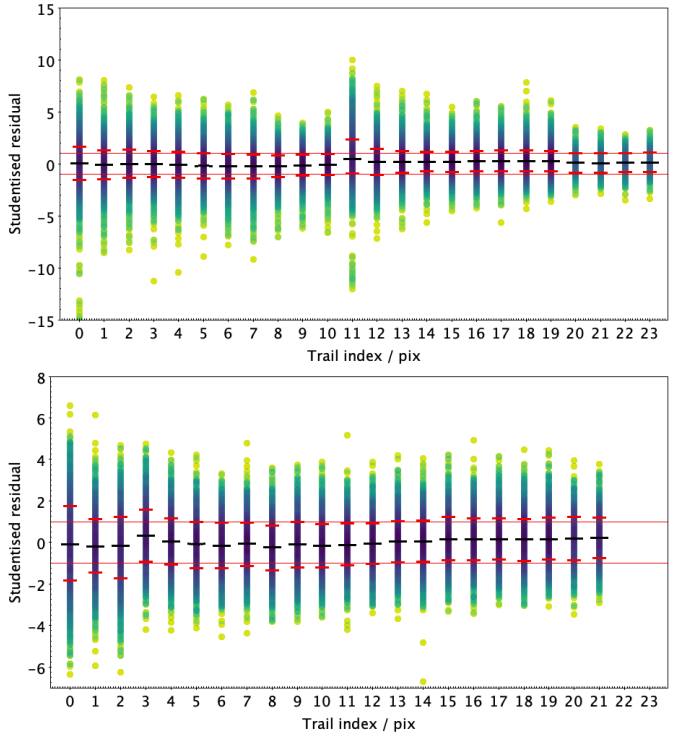

Fig. 10. Studentised (unit-weight error) residuals as a function of trail position for all three-trap species calibrations. Upper panel: blue variant (AF+BP) devices. Lower panel: red variant (RP) devices. The thick dashed lines indicate the 16%, 50%, and 84% (red, black, and red) quantiles, which correspond to the distribution median $\pm 1\sigma$. The thin red lines show the ± 1 expected position assuming normally distributed uncertainties.

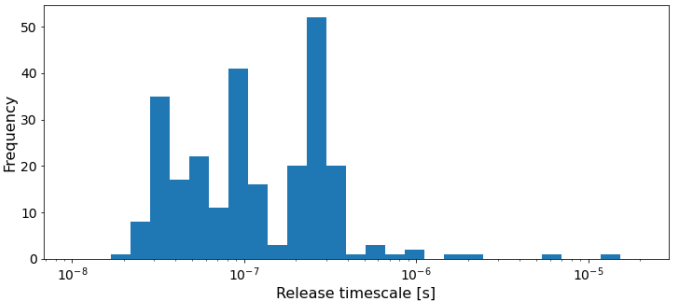

Fig. 11. Distribution of trap release-timescale values from the final three-trap species calibrations, calculated from the best-fit trap energy values of the calibration activity at epoch OBMT = 8224 revolutions. Three well-defined peaks for the different species of the `CtiPixel` model are present, including the fastest manufacturing species that dominated the CCD defects at launch and two slower radiation-induced traps. A tail of slower emission times can be observed for the third species. These can be interpreted as emerging defects still in an unstable configuration, similarly to the radiation-induced defects measured on board the *Euclid* mission CCDs.

to indicate a pair of CCDs manufactured from the same silicon wafer; the *(ROW3, AF9)* pair is *(ROW2, AF4)*, whose fit presents a typical GoF value). Appendix D in Rowell et al. (2026) presents a list of *Gaia* CCD twins and information on the device types.

With respect to β, the charge volume coefficient, the parameter that in `CtiPixel` links the number of signal electrons with the confinement volume (the physical volume filled by the charge packet in a pixel), the measured distribution for the third trap

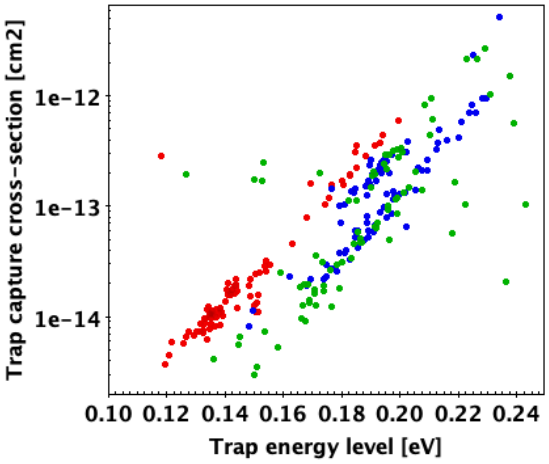

Fig. 12. Scatter plot of the trap capture cross sections [cm^2] vs. energy level [eV] for the model fits of the three-trap species to the entire *Gaia* mission dataset. The red, green, and blue dots are relative to the first, second, and third trap species in the `CtiPixel` model fit.

species appears to separate from the other types of defects. This result could indicate a different physical distribution of this trap species within the pixels, and could indeed suggest that these defects are still migrating in the lattice and have not yet bonded into a stable defect.

Another interesting result to note in these plots is the different parameter space occupied by the red variant (RP) devices with respect to the blue CCDs, in terms of both the energy levels (and hence release timescale) and the trap cross sections. This result is not well understood. As shown in Fig. 8, the number of manufacturing defects in the serial register was lower in red devices at launch, while the rate of traps increase appears similar for all devices (see also Ahmed et al. 2020). This hints to possible differences in the distribution of the impurities during the manufacturing process of thicker and thinner devices, even if both the pixels architecture and the serial readout process are common to all devices.

The fits to the calibration datasets occasionally show systematic effects in the residuals in the very first pixels of the charge trails, as mentioned previously. Effects such as an inaccurate subtraction of the CCD bias or charge blooming from the high injected signal flux in the last pixel of the serial register seem unlikely causes of the residuals. For instance, such a blooming effect is not detected in the first pre-scan pixel. The most plausible explanation of the poor fits is an inadequacy in the `CtiPixel` implementation, possibly too simplistic, in modelling the full range of the trap emission timescales. Once again, the intrinsic limitation of a charge distortion modelling that allows only a small number of trap species with distinct trap parameters could be the cause of the limited success of `CtiPixel` to fully account for all the observed CTI effects.

The `CtiPixel` model was developed with the main goal of characterising the defects responsible for the effects of serial CTI in *Gaia* CCDs and to measure the evolution of radiation damage at L2. Trying to apply the model, calibrated using engineering data, to science observations is a challenging endeavour for a number of reasons. For instance, the PSF needs to be sampled fully in 2D for all predicted sources. Processing of science data would require predicting the scene of each science window to account for any other signal that might affect the history of the traps and their occupancy level, including background variations. The scene outside the PSF core would inevitably be poorly

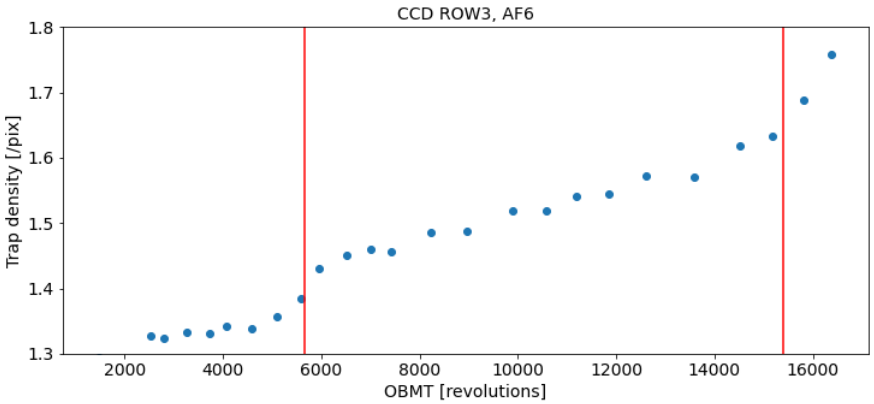

Fig. 13. Evolution of the total density of traps for the CCD in row 3 and AF strip 6. The observed trend is caused by a gradual increase in damage caused by cosmic rays and sudden step jumps in correspondence to solar flares event, shown as the red lines for the class X8.2 flare of September 2017 and as the start of the intense period of solar activity during 2024.

characterized, as the mid-to-far PSF wings are not well-covered by calibration data. This would be problematic in the serial CTI context, where the wings in the Across Scan direction are most important. A proper application of the serial CTI model would also need to account for other CCD response effects, such as the column response non uniformity, when realising the predicted scene. The readout sequencing of science data would be critical in the application of the CTI model, but this aspect might not have been well-constrained by the calibrations using only engineering sequences.

In the attempt to apply the calibrated `CtiPixel` model for science data processing, the PSF model was used in combination with the background modelling and other auxiliary calibrations such as the bias non-uniformity corrections to estimate the science inputs, applying the `CtiPixel` algorithm to derive a complete model of a selected sample of observations, including serial CTI. The results of the application were only partially satisfactory, as the calibrated model reproduced qualitatively the serial CTI signature observed in the science windows but could not fully model its effects under all conditions. In particular, the model struggled to reproduce the observed CTI effects for very bright sources and in the case of high local background, where the diffuse distribution of charge over a device mitigates the losses due to traps.

The result points to possible limitations with the accuracy of the `CtiPixel` model and its calibration with the sole use of the dedicated serial CTI charge injection activities. It is possible, for example, that the limited number of post-scan pixels for which the charge trail flux values are recorded is insufficient to identify trap species of longer time emission constants that might be present in the serial register and affect the readout. A second intrinsic limitation of the calibration using post-scan trails is that only the integrated effect of the damage is measured, based on which the average density of traps in the serial register can be derived; in reality, an accurate model for the treatment of serial CTI for stars and other point sources requires the estimate of the density of traps in each pixel, to account for its spatial non-uniformity (both of the initial manufacturing defects and of the traps accumulating due to radiation damage). The assessment of the accuracy of the `CtiPixel` model, when applied to images affected by radiation damage, could have been hindered by other systematic effects that were not fully calibrated at the time science validation was attempted. This is for example the case of the brighter/fatter effect, which can result in image residuals of the same order as the ones caused by serial CTI. Furthermore, it is worth noting how the PSF model does not actually represent the purely linear part of the signal, as real science observations, which present a certain level of serial CTI depending on their signal level and the specific AC position on the detector, are used for its calibration. The attempted science tests were therefore not ideally suited to reproduce the exact scenario for which `CtiPixel` was designed and developed.

A critical aspect already mentioned earlier that was experienced when attempting the processing of the test science datasets with `CtiPixel` is the high demand of computation resources needed when modelling the image readout at the pixel level. After these initial, and not fully successful test cases, it was concluded that the integration of the `CtiPixel` task into the *Gaia*'s Image Parameter Determination software (IPD) for the treatment of the CTI distortion effects would not be feasible, as it would exceed the accessible machine processing time, considering the sheer volume of *Gaia* observations and the cyclic nature of the data reduction. It is also worth noting that, in the *Gaia* context, the AC location bias caused by serial CTI are not as critical as the CTI bias in the parallel direction, since the AC source locations are not used in the AGIS astrometric solution (Lindegren et al. 2016), and are only indirectly employed in the attitude and calibration solutions. The efforts with the characterisation and the analysis of CTI were therefore ultimately redirected to a project to report passively on the observed biases, without attempting any processing of science data.

8. Conclusions

The 106 CCDs of ESA's *Gaia* spacecraft have been exposed to the particle irradiation of the space environment during the course of the 11-year mission. Dedicated serial CTI calibration engineering activities, performed periodically on board the spacecraft, have been used to measure the effect of radiation damage on the detectors and to monitor its evolution. A pixel-based physically motivated `CtiPixel` model that adopted the Shockley-Read-Hall theory of charge traps was developed to analyse the serial CTI calibration datasets. The results of the investigation showed that alongside the manufacturing defects already present at launch, new trap species caused by particle irradiation have emerged. The newly generated defects are characterised by longer charge-release timescales compared to the

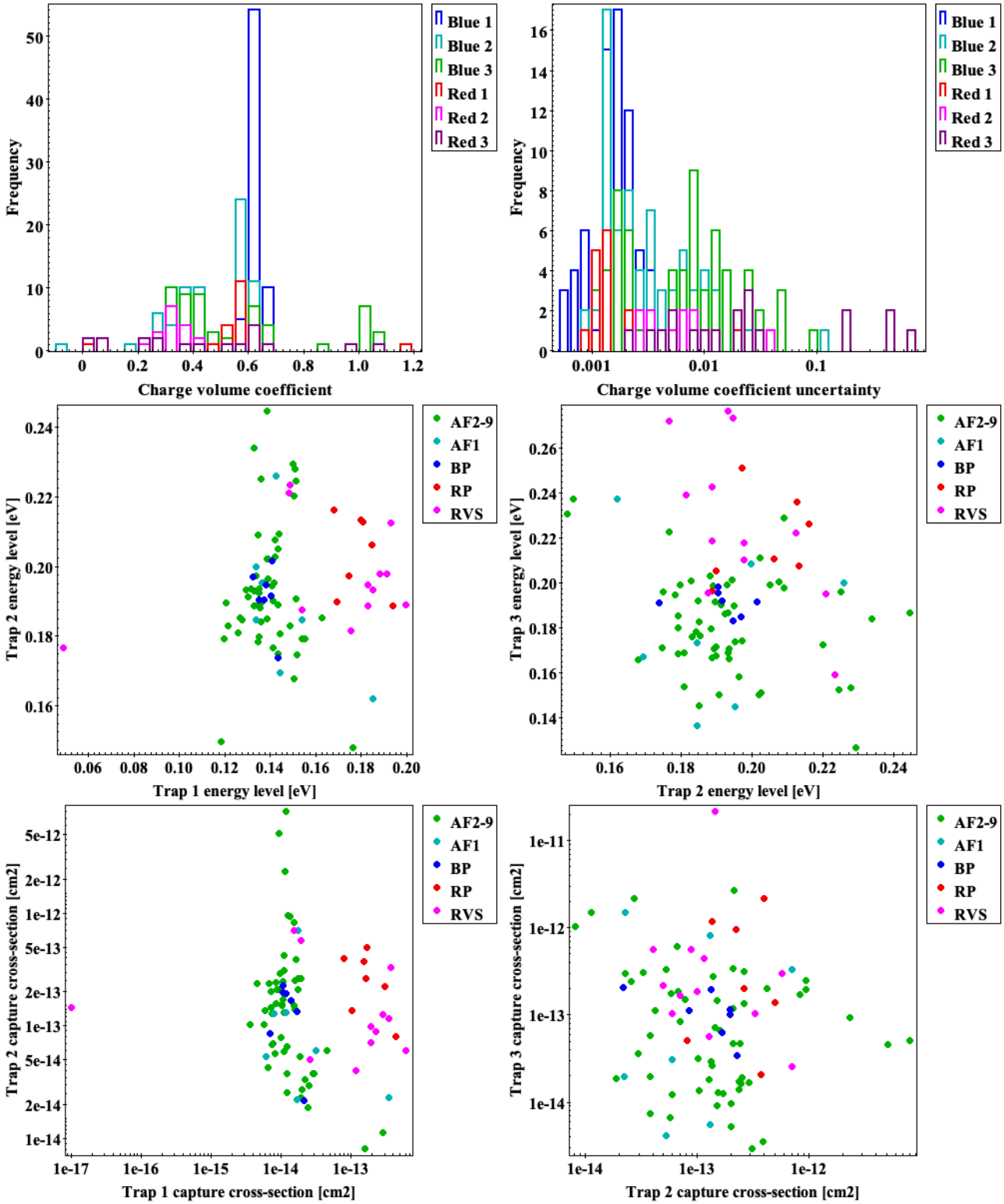

Fig. 14. Trap parameters for the final three-trap species calibrations plotted as histograms (charge volume confinement exponent β; top row) and scattergrams (trap species energy level E_t, middle row; trap capture cross-section parameter α, bottom row) for the full calibration datasets.

original manufacturing defect. The measured energy level of the intermediate trap is consistent with the known value of the multi-vacancy defect, while the third species presents a tail in its release-time distribution, which is suggestive of a dynamical transitional state of some radiation-induced traps, with defects not fully settled into their final configuration. The evolution of the radiation-induced serial damage appears to be linear, with the exception of calibration epochs following a strong CME directed towards Earth, such as those that occurred in 2017 and 2024, which presented a step increase in the damage level. The latest epochs also show the effects of temperature instabilities of the focal plane on the measured serial CTI, and a further step

increase caused by the engineering CCD annealing test carried out after the end of *Gaia* science operations.

Acknowledgements. This work has made use of data from the European Space Agency (ESA) mission *Gaia* (https://www.cosmos.esa.int/gaia), processed by the *Gaia* Data Processing and Analysis Consortium (DPAC, https://www.cosmos.esa.int/web/gaia/dpac/consortium). Funding for the DPAC has been provided by national institutions, in particular the institutions participating in the *Gaia* Multilateral Agreement. The *Gaia* mission website is: http://www.cosmos.esa.int/gaia. This work was financially supported by the European Space Agency (ESA) in the framework of the Gaia project; and the United Kingdom Space Agency (UKSA) through the following grants to the University of Edinburgh and the University of Leicester, ST/S000976/1, ST/S001123/1. The authors gratefully acknowledge the use of computer resources from MareNostrum, and the technical expertise and assistance provided by the Red Española de Supercomputación at the Barcelona Supercomputing Center, Centro Nacional de Supercomputación. Diagrams were produced using the astronomy-oriented data handling and visualisation software TOPCAT (Taylor 2005).

References

Ahmed, S., Hall, D., Crowley, C., et al. 2020, in X-Ray, Optical, and Infrared Detectors for Astronomy IX, 11454, eds. A. D. Holland, & J. Beletic, International Society for Optics and Photonics (SPIE), 114540S
Bautz, M., Prigozhin, G., Kissel, S., et al. 2005, IEEE Trans. Nucl. Sci., 52, 519
Crowley, C., Abreu, A., Kohley, R., Prod'homme, T., & Beaufort, T. 2016a, SPIE Conf. Ser., 9915, 99150K
Crowley, C., Kohley, R., Hambly, N. C., et al. 2016b, A&A, 595, A6
Euclid Collaboration (Cropper, M., et al.) 2025a, A&A, 697, A2
Euclid Collaboration (Mellier, Y., et al.) 2025b, A&A, 697, A1
Gaia Collaboration (Prusti, T., et al.) 2016, A&A, 595, A1
Garmire, G. P., Bautz, M. W., Ford, P. G., Nousek, J. A., & Ricker, Jr., G. R. 2003, SPIE Conf. Ser., 4851, 28
Hall, D. J., Murray, N. J., Holland, A. D., et al. 2014, IEEE Trans. Nucl. Sci., 61, 1826
Hambly, N. C., Cropper, M., Boudreault, S., et al. 2018, A&A, 616, A15
Hopkinson, G. R., C. J. Dale, C. J., & Marshall, P. W. 1996, IEEE Trans. Nucl. Sci., 43, 614
Hopkinson, G., Short, A., Vetel, C., Zayer, I., & Holland, A. 2005, IEEE Trans. Nucl. Sci., 52, 2664
Janesick, J. R. 2001, Scientific charge-coupled devices
Kohley, R., Crowley, C. M., Garé, P., et al. 2014, SPIE Conf. Ser., 9154, 915406
Lindegren, L., Lammers, U., Bastian, U., et al. 2016, A&A, 595, A4
Lindegren, L., Hernández, J., Bombrun, A., et al. 2018, A&A, 616, A2
Marshall, P., Dale, C., Burke, E., Summers, G., & Bender, G. 1989, IEEE Trans. Nucl. Sci., 36, 1831
Monmeyran, C., Patel, N. S., Bautz, M. W., et al. 2016, Nuclear Instruments and Methods in Physics Research Section B: Beam Interactions with Materials and Atoms, 389, 23
Rowell, N., Davidson, M., Hambly, N. C., et al., 2026, A&A, submitted
Seabroke, G. M., Prod'homme, T., Murray, N. J., et al. 2013, MNRAS, 430, 3155
Seaton, D. B., & Darnel, J. M. 2018, ApJ, 852, L9
Shockley, W., & Read, W. T. 1952, Phys. Rev., 87, 835
Short, A., Hopkinson, G., Laborie, A., et al. 2005, SPIE Conf. Ser., 5902, 31
Short, A., Crowley, C., de Bruijne, J. H. J., & Prod'homme, T. 2013, MNRAS, 430, 3078
Skottfelt, J., Wander, M., Gai, M., et al. 2024, SPIE Conf. Ser., 9150
Srour, J., & McGarrity, J. 1988, Proc. IEEE, 76, 1443
Taylor, M. B. 2005, in Astronomical Society of the Pacific Conference Series, 347, Astronomical Data Analysis Software and Systems XIV, eds. P. Shopbell, M. Britton, & R. Ebert, 29
van Lint, V. A. J. 1963, IEEE Trans. Nucl. Sci., 10, 11
Watkins, G. D., & Corbett, J. W. 1964, Phys. Rev., 134, A1359

Appendix A: End of Life test

Gaia scientific observations ended on 15 January 2025. The spacecraft was moved from its position around L2 into a retirement heliocentric orbit with a final burn of its thrusters on 27 March 2025, and passivated. Before this final procedure, a series of engineering and technology tests were conducted to investigate the instruments and spacecraft behaviour, to improve calibrations and inform future missions. Among these tests, of importance for radiation damage and CTI studies was the CCD radiation damage annealing test.

During the annealing procedure, on 6 March 2025 the temperature of the focal plane was increased to room temperatures (in a range between 27 and 38 degrees Celsius across the focal plane) for the duration of four spacecraft revolutions (corresponding to approximately a full day). The expected outcome of the test was a partial reduction of the measured CTI, in particular in the parallel direction, as most traps in the image area have been induced by on-orbit irradiation at cold temperatures. In the serial register, where most of the traps even at the end of the mission are still the original manufacturing defects already present at launch a lower improvement in CTI was expected, as the O-V (oxygen-vacancy) defect is known to be stable below 150 C (Janesick 2001).

Two days later, at OBMT revolution 16638, a final serial CTI calibration activity was conducted, allowing the investigation of the effect of the bakeout on the *Gaia* devices. This EoL serial calibration activity was conducted following the same procedure as all the previous pre-annealing epochs, injecting charge in blocks at a number of different injection levels. The dataset collected from the final epoch could therefore be processed following the same procedure already described for the earlier datasets, but limiting the fit to the data of the single EoL epoch. With this choice, any change in the traps parameters could be measured and compared to previous epochs, specifically in regard to the density of the species and any rearrangement of their energy levels. Two major changes were measured following the bakeout: in the parallel direction, a reduction of the effects of CTI of approximately 30% was observed, as derived from the analysis by *Gaia* payload experts (private communication); inversely, and maybe unexpectedly, in the serial direction a reverse-annealing effect was seen, with an increase in the measured density of defects.

The clear evidence of an increase in the trap densities after the CCD annealing test is observed from the evolution of the best-fit parameters, as shown in Fig. A.1, for the blue and red devices (top and bottom plots). In detail, while the density of the manufacturing defects (red circles) appears to be stable after the bakeout, a clear step is seen for the two radiation-induced species, for both types of devices. The outcome of the bakeout procedure seems to point to a partial rearrangement of the defects caused by space radiation, with the formation of new stable defects with a characteristic release timescale that is able to affect the readout at the serial clocking frequency. On the other hand, for the manufacturing defects, already present at launch and that formed at room temperatures, the annealing test temperature wasn't sufficiently high to affect their bonding with the Oxygen impurities (bakeout temperatures of approximately 600 K are indeed needed to anneal the O-V defect). This result is reminiscent of the outcome of the annealing procedure that was attempted on board NASA's *Chandra* X-ray observatory, following the sharp increase of CTI measured in the Front Illuminated advanced CCD Imaging Spectrometer (ACIS; Garmire et al. 2003) shortly after launch, caused by the exposure to soft

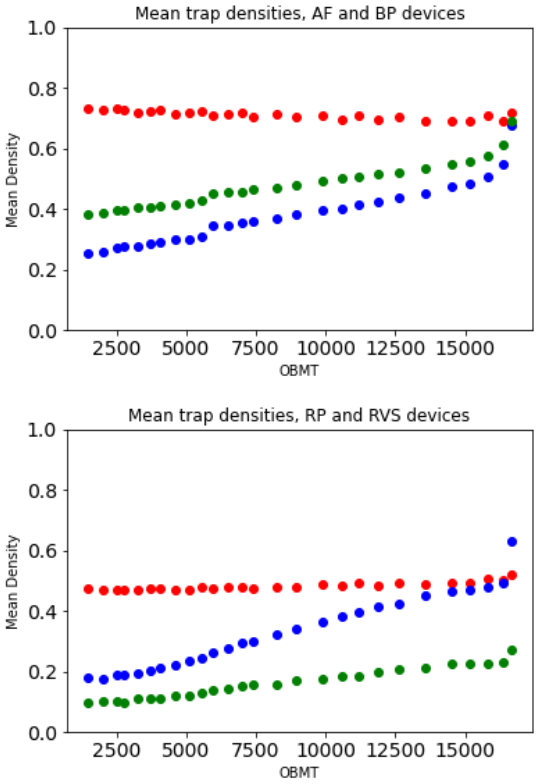

Fig. A.1: Time evolution of the mean densities of the three trap species over the entire mission, for all blue devices (AF and BP, top panel), and for the red devices (RP and RVS, bottom panel). A clear step in the density of the radiation-induced traps is seen for both the blue and the red devices, while the density of the manufacturing trap appear unaffected by the annealing procedure.

proton. The *Chandra* focal plane was heated from the nominal operating temperature of -100 C to +30 C, in an attempt to alleviate the observed CTI increase, but the process resulted in a further increase of CTI, attributed to the formation of new defects caused by Carbon impurities in the ACIS CCDs (Bautz et al. 2005; Monmeyran et al. 2016).

Figure A.2 compares the distribution of the energy levels of the three trap species derived from the fits of the pre- and post-annealing epochs. While the distributions of the fitted energy levels of the manufacturing trap (the first species) and the intermediate trap species appear similar before and after bakeout, the energies of the slower species appear slightly shifted in the EoL epoch, and with a tail towards higher energies. This finding could be interpreted as an indication of a partial rearrangement of these defects to a new configuration after the interval at higher temperatures.

The lines immediately following the injection blocks of the serial calibration activities can inform on the level of CTI damage in the parallel direction, as their flux, after the appropriate bias and background have been subtracted, consist of deferred charge by traps in the image section of the CCDs. This analysis revealed a reduction of approximately 25–30% in the amount of deferred charge after the EoL annealing procedure. This outcome is consistent with expectations, as most traps causing parallel readout charge losses have formed in orbit at cold temperatures, and the focal plane bakeout has resulted in the partial annealing of the unstable defects.

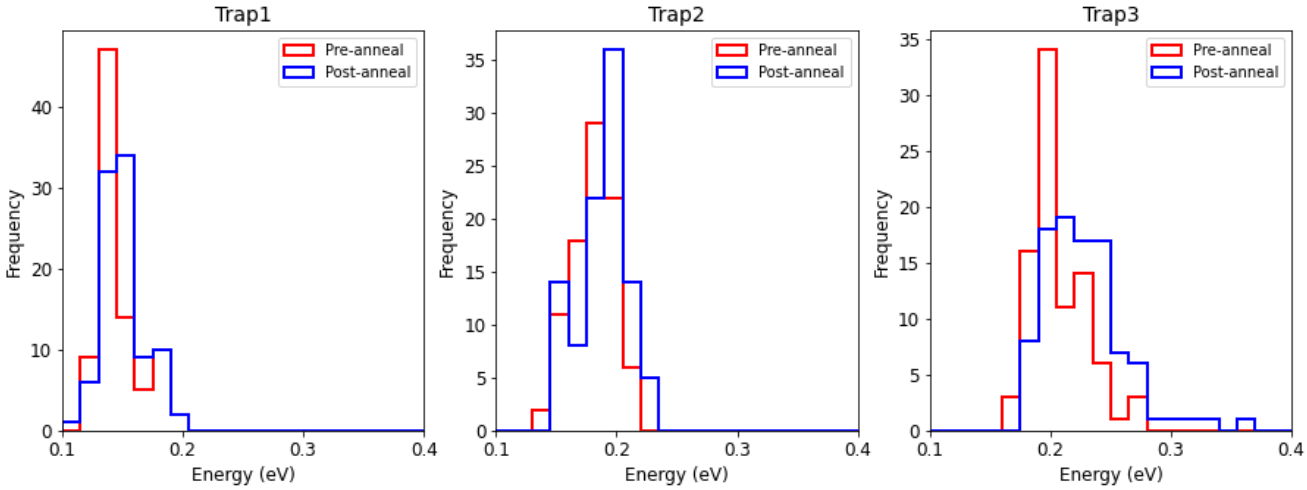

Fig. A.2: Distribution of the characteristic energy levels of the three trap species, from the best fit from the pre- and post-annealing epochs (from left to right: first, second, and third species).